NANO LETTERS

pubs.acs.org/NanoLett Letter

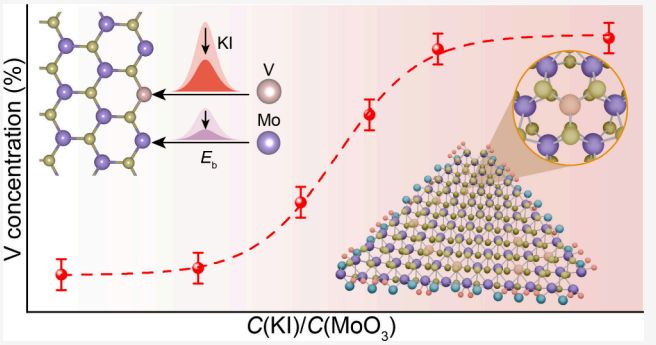
Boltzmann Sigmoidal Modulation of Vanadium Doping in Monolayer MoS_2 by Potassium Iodide

Yuanyuan Qiu,[#] Bin Hua,[#] Zhenping Wang,[#] Fei Hu,[#] Dong Zhang, Yang Lu, Marvin L. Cohen, Alex Zettl, Kecheng Cao, Cong Su,* Young Woo Choi,* and Qingqing Ji*

Cite This: https://doi.org/10.1021/acs.nanolett.6c03019 Read Online

ACCESS | Metrics & More | Article Recommendations | Supporting Information

ABSTRACT: The atomic thickness of two-dimensional (2D) semiconductors makes conventional postgrowth substitutional doping highly challenging. Instead, such atomic substitution can be more effectively achieved *in situ* through chemical vapor deposition synthesis. However, the mechanistic details governing this growth process have remained poorly understood. Using V-doped monolayer MoS_2 as a model system, this work elucidates its growth mechanism and doping tunability facilitated by a potassium iodide (KI) promoter. A Raman spectroscopic probe, established through correlation with scanning transmission electron microscopy, was developed to quantify the V dopant concentration and distribution uniformity. Systematic growth experiments and detailed characterizations revealed that doping saturation levels were significantly below the precursor feeding ratio. This saturation phenomenon could be modulated by KI dosage following a Boltzmann sigmoid function, indicative of an iodide-activated doping mechanism compatible with the edge passivation substitution (EPS) model. Our findings advance the doping theory in low-dimensional systems and provide essential insights into achieving controlled heteroatom substitution in 2D semiconductors.



KEYWORDS: *2D semiconductors, MoS_2, substitutional doping, Raman spectroscopy, halide activation*

Substitutional doping has played a pivotal role in semiconductor electronics,[1−3] enabling modulation of the charge carrier polarity and construction of the complementary metal-oxide-semiconductor (CMOS) circuits. This doping capability is equivalently important for two-dimensional (2D) semiconductors[4,5] such as monolayer transition metal dichalcogenides (TMDs), which are immune to short-channel effects[6,7] and hold promises for ultrascaling the CMOS technology and extending the Moore's law.[8,9] Furthermore, heteroatom-substituted monolayer TMDs (e.g., V-doped MoS_2 and WSe_2) are theoretically predicted to be candidate 2D dilute magnetic semiconductors with high Curie temperatures,[10−12] and experimental evidence has recently been observed;[13,14] albeit, there are some uncertainties. The magnetoelectric coupling in such 2D systems, combined with their excellent gate tunability, can potentially spur a wealth of electronic[15,16] and spintronic applications[17] that show supremacy in advanced node regimes.

The atomic thinness of the 2D semiconductors, however, precludes ion implantation,[18] the substitutional doping strategy for conventional 3D semiconductors, to be effective in the 2D case,[19] where defect creation rather than ion substitution more likely occurs due to the bombardment effect. A feasible doping strategy for such monolayer materials is *in situ* doping during their growth.[20,21] This necessitates engineering on the reactivity of growth precursors for both the dopant and the host material as well as the thermodynamics that govern clustering/dispersion of the heteroatoms and hence the doping uniformity. In this sense, halide salts (e.g., NaCl and KI) known to promote chemical vapor deposition (CVD) growth of a wide range of 2D TMDs[22,23] can be a potential knob for achieving the desired doping tunability. The key to the promoting effect lies in the formation of volatile oxyhalides as the precursor[23] or, equivalently, the competitive passivation of TMD edges by oxygen and/or halogen atoms, known as the edge passivation substitution (EPS) model.[24] Nevertheless, for doped growth of 2D TMDs, the correlation of halide promoters to doping tunability has yet to be established, and the effectiveness of the EPS model in this case still needs justification.

Received: June 19, 2026
Revised: September 27, 2026
Accepted: September 29, 2026

ACS Publications © XXXX American Chemical Society

Downloaded from pubs.acs.org/halefd/article-pdf/doi/10.1021/acs.nanolett.6c03019/6874322/acs.nanolett.6c03019.pdf by SOGANG UNIV user on 06 October 2026

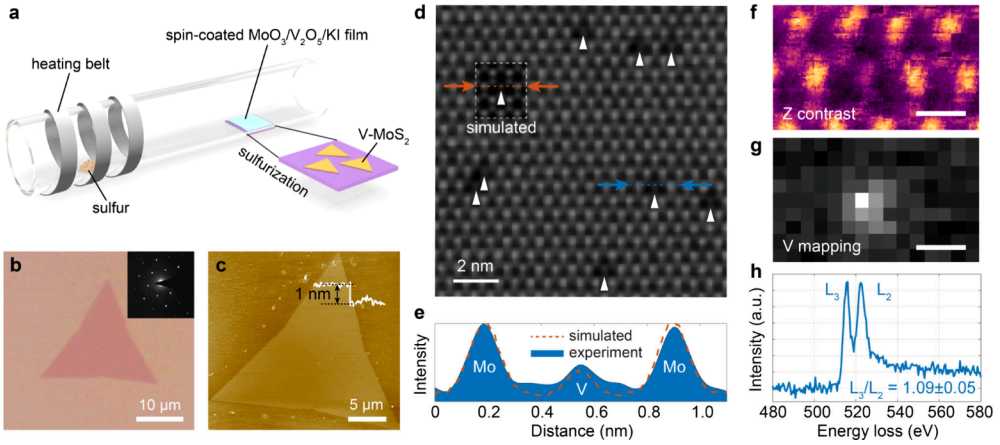


Figure 1. Synthesizing V-doped MoS_2 (V-MoS_2) monolayers and the atomic characterizations. (a) Schematic illustration of the growth setup by sulfurizing precoated MoO_3/V_2O_5/KI films in a quartz tube with two-zone temperature control. (b) The optical image and (c) AFM height image of the monolayer V-MoS_2. Inset in (b): selective area diffraction pattern. (d) Atomic-resolution ADF STEM image of the monolayer V-MoS_2 with V dopants marked by white arrows. A simulated image of V-doped MoS_2, enclosed by the dashed rectangle, is overlapped with the experimental image. (e) The line profiles along dashed blue line and the dashed orange line in (d). (f) The ADF image and (g) the corresponding EELS mapping, confirming the V atoms. The scale bars in (f) and (g) are 0.3 nm. (h) Single-atom EELS of V dopant showing a white line ratio between L_3 and L_2 peaks to be around 1.09.

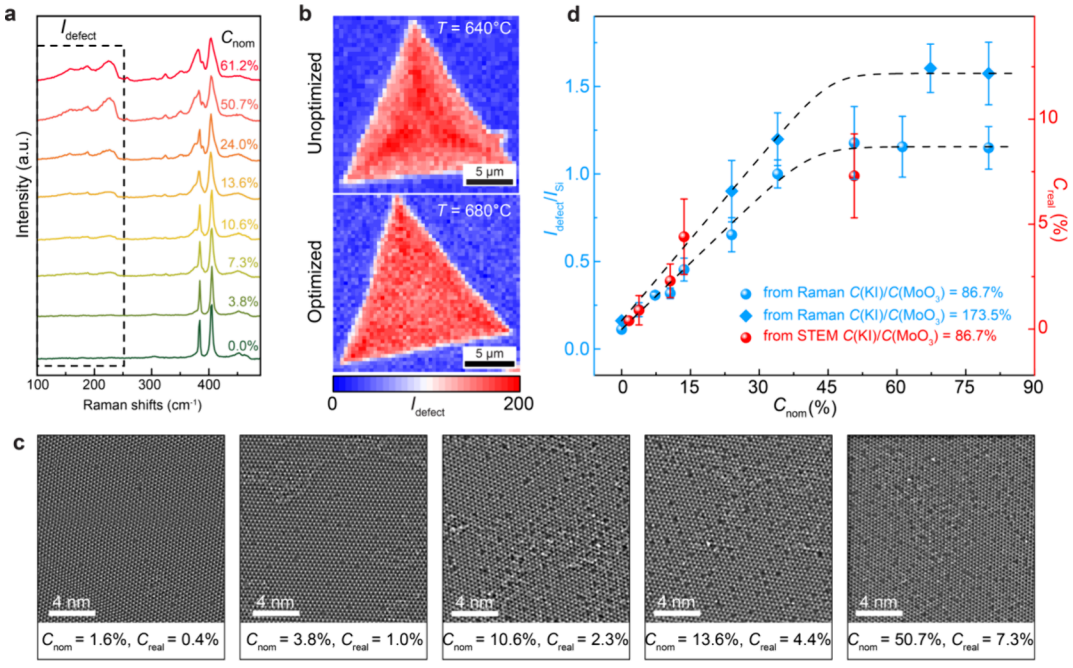


Figure 2. Raman spectra for probing the real concentration of V dopant. (a) Evolution of the Raman spectra with increasing C_{nom}. The concentration of KI is kept constant at $C(KI)/C(MoO_3)$ = 86.7% for all these cases. (b) I_{defect} mapping of samples grown at 640 °C (upper panel) and 680 °C (lower panel), showing improved spatial uniformity at 680 °C. (c) Correlating the real concentration, C_{real}, via STEM images of samples with different nominal concentrations, C_{nom}, at 1.6%, 3.8%, 10.6%, 13.6%, and 50.7%. All ADF images are 16 nm × 16 nm with postprocessing to highlight the V dopants. (d) The plot shows normalized V-dopant-associated Raman intensity I_{defect}/I_{Si} at $C(KI)/C(MoO_3)$ = 86.7% (blue circles, up to $C(V_2O_5)/C(MoO_3)$ = 2.0, i.e., $C_{nom} \approx 80\%$) and 173.5% (blue diamonds, including the V-free control plotted at C_{nom} = 0) on the left axis together with the STEM-derived C_{real} at 86.7% (red circles) on the right axis, as functions of C_{nom}. The C_{real} error bars in (d) represent the standard deviation across the 8 × 8 nm^2 subregions within the 64 × 64 nm^2 STEM overview fields analyzed for each C_{nom} condition at $C(KI)/C(MoO_3)$ = 86.7%. Error bars on the Raman data represent the mean ± s.d. of repeated Raman measurements on each sample.

In this work, we exploit the growth of V-doped monolayer MoS_2 (V-MoS_2) as a model system to showcase how an iodide salt (KI) can modulate the utilization of the dopant precursors and hence the density and uniformity of the V heteroatoms in the host MoS_2 lattice. The doping density, as indicated by the Raman spectroscopic probe and calibrated by scanning transmission electron microscopy (STEM), exhibits a Boltzmann sigmoidal dependence on the concentration of the KI. This suggests a KI-activated doping mechanism that can be reconciled theoretically within the EPS framework. Our findings highlight the critical role of halide salts in the doping tunability in 2D semiconductors and propel the development of the doping theory for low-dimensional materials.

https://doi.org/10.1021/acs.nanolett.6c03019
Nano Lett. XXXX, XXX, XXX−XXX

Downloaded from pubs.acs.org/naletd/article-pdf/doi/10.1021/acs.nanolett.6c03019/6874322/acs.nanolett.6c03019.pdf by SOGANG UNIV user on 06 October 2026

The CVD growth of monolayer V-MoS_2 involves spin-coating of the liquid-phase precursor (ammonia solution dissolving a designed combination of MoO_3, V_2O_5, and KI) onto a SiO_2/Si substrate, followed by a high-temperature sulfurization process, as schematically shown in Figure 1a. More growth details can be found in Supporting Information. Single-domain flakes in shapes of concave triangles are formed on the substrate (Figure 1b) with a monolayer thickness of ~1 nm (Figure 1c). Through medium-angle annular dark-field STEM (MAADF-STEM), atomic-resolution imaging of monolayer V-MoS_2 was achieved, identifying the doping sites of V atoms with lower contrasts than Mo (indicated by white arrows in Figure 1d), distinct from other atomic defects observed (Figure S1). To verify the accuracy of the doping configuration, the theoretically simulated image of V substituting Mo sites (within the dashed box) was overlaid with the experimental image, showing a high degree of consistency in both atomic arrangement and intensity distribution (Figure 1d). Further line scan analysis (Figure 1e) demonstrates that the intensity reduction on the V dopant in the experimental curve (blue dashed line) matches the simulated one (orange dashed line), confirming that V atoms occupy Mo lattice sites substitutionally rather than interstitially or in clusters.

The simultaneously acquired atomic-resolution ADF image (Figure 1f) and vanadium elemental surface distribution map (Figure 1g) reveal that the signal from V atoms (white spots in Figure 1g) strictly corresponds to darker lattice positions. Single-atom electron energy loss spectroscopy (EELS) analysis (Figure 1h) and the corresponding simulation (Figure S2) further elucidates the chemical state of vanadium. Detailed information on EELS acquisition, data processing, and spectral simulation is provided in the Methods Section of the Supporting Information. The L_3/L_2 white line intensity ratio (~1.09) closely matches the typical value for V^{4+} (1.0−1.2), indicating that V substitutes Mo sites in the +4 valence state[25,26] without deficient sulfur or additional oxygen bonding in this scanned region. These results directly confirm the substitutional doping of V atoms at the atomic scale and rule out other possible doping configurations, although further site-resolved EELS measurements across a broader doping range are needed to clarify whether the V chemical state varies with dopant concentration.

A Raman spectroscopic probe was then established to characterize the V doping density and uniformity at micrometer scales. To do this, Raman spectra for V-MoS_2 of varied nominal doping concentrations (C_{nom}, the feeding atomic ratios of V/(V + Mo) in precursors) were experimentally collected (Figure 2a), and a group of convoluted peaks in the range of 100−250 cm^{-1} were intuitively identified in positive correlation with C_{nom}: the integrated intensity of these peaks (I_{defect}) increases monotonically as C_{nom} increases. In contrast, an undoped sample grown with a nominal $C(KI):C(MoO_3)$ = 1:1 ratio shows no comparable low-frequency features, whereas an undoped MoS_2 control grown under an excess-KI powder-source condition exhibits volatile Raman features distinct from the V-associated defect bands (Figure S3). Previous work has reported that halide salts predominantly accumulate at the MoS_2−substrate interface and interact only weakly with MoS_2 with potassium-related XPS signals no longer detected after sample transfer.[27] We note that I_{defect} could lack spatial uniformity for samples grown at the temperature of 640 °C, despite the preserved triangular single-crystal shapes (upper panel in Figure 2b). This suggests different utilization efficiencies of V and Mo atoms in constructing the monolayer lattice. Nevertheless, V-MoS_2 grown at 680 °C exhibits uniform I_{defect} distribution (lower half in Figure 2b) and can be used for finding the one-to-one correspondence to the real doping concentration (C_{real}) determined by STEM.

Figure 2c exhibits atomic-resolution ADF images (each of 16 × 16 nm^2) for V-MoS_2 samples with varied C_{nom}. Corresponding C_{real} values are also shown at the bottom of each ADF image. Details of the Fourier-filtering and ADF-intensity-based V-site identification procedure are provided in the Supporting Information, and a representative raw and processed overview field is shown in Figure S4. For each C_{nom} condition, STEM quantification was performed using 64 × 64 nm^2 overview fields partitioned into 8 × 8 nm^2 subregions. Representative distributions of the V atom areal density across the analyzed subregions are shown in Figure S5. STEM fields were selected from Raman-uniform regions away from flake edges with the sampling and analysis procedures described in the Supporting Information. Nearest-neighbor analysis provided no statistically significant evidence of V clustering or anticlustering across the analyzed data sets ($|Z| < 2$; Table S1).

At a fixed KI dosage of $C(KI)/C(MoO_3)$ = 86.7%, the normalized I_{defect} and STEM-derived C_{real} values were plotted against C_{nom} in Figure 2d. Raman acquisition and processing details are provided in the Supporting Information. The left and right axes were scaled to facilitate comparison, using a scaling factor obtained from a linear fit of I_{defect} against C_{real}. Two regimes were evident: At low doping levels (C_{nom} < 15%, C_{real} < 2.5%), C_{real} increased approximately linearly with C_{nom} with a V atomic yield, defined as $\eta = C_{real}/C_{nom}$, of approximately 17%. At C_{nom} > 45%, C_{real} approached an experimentally observed plateau of approximately 9%, while η decreased markedly. This C_{real} plateau applies to the specific $C(KI)/C(MoO_3)$ = 86.7% growth condition and should not be interpreted as a universal lattice-doping limit. The low atomic yield indicates that most of the nominally supplied V was not substitutionally incorporated into the MoS_2 lattice. Possible fates of the unincorporated V may include retention on the substrate as vanadium oxide particles or other V-containing residues, as well as transport out of the growth zone in the form of volatile V-containing species during high-temperature growth.[15]

To examine whether this loading dependence is affected by the KI dosage, an additional Raman series acquired at $C(KI)/C(MoO_3)$ = 173.5% is included in the same plot. The higher-KI Raman series generally show larger I_{defect} values at comparable C_{nom} ($C(V_2O_5)/C(MoO_3)$ = 0.16, 0.26; C_{nom} ≈ 24%, 34%) and a similar tendency toward saturation at high C_{nom} ($C(V_2O_5)/C(MoO_3)$ = 1.03, 2; C_{nom} ≈ 67%, 80%). The $I_{defect}-C_{real}$ calibration established at $C(KI)/C(MoO_3)$ = 86.7% was validated at this high KI dosage, predicting a Raman-inferred C_{real} of 11.3−13.6% for $C(V_2O_5)/C(MoO_3)$ = 1.03 (C_{nom} ≈ 67%). The predicted range encompasses the STEM-quantified C_{real} of 11.5% and 12.3% for the same-batch samples (Figure S6; Table S2), supporting the transferability of the $I_{defect}-C_{real}$ relationship across the KI series. This is naturally expected in our samples, whose atomic defects are dominated by the substitutional V heteroatoms: a higher KI dosage promotes V incorporation and thus raises I_{defect}, but it does not change the Raman response per incorporated V atom. These results demonstrate the viability of using I_{defect} to reflect the

Downloaded from pubs.acs.org/naletd/article-pdf/doi/10.1021/acs.nanolett.6c03019/6874322/acs.nanolett.6c03019.pdf by SOGANG UNIV user on 06 October 2026

https://doi.org/10.1021/acs.nanolett.6c03019
Nano Lett. XXXX, XXX, XXX−XXX

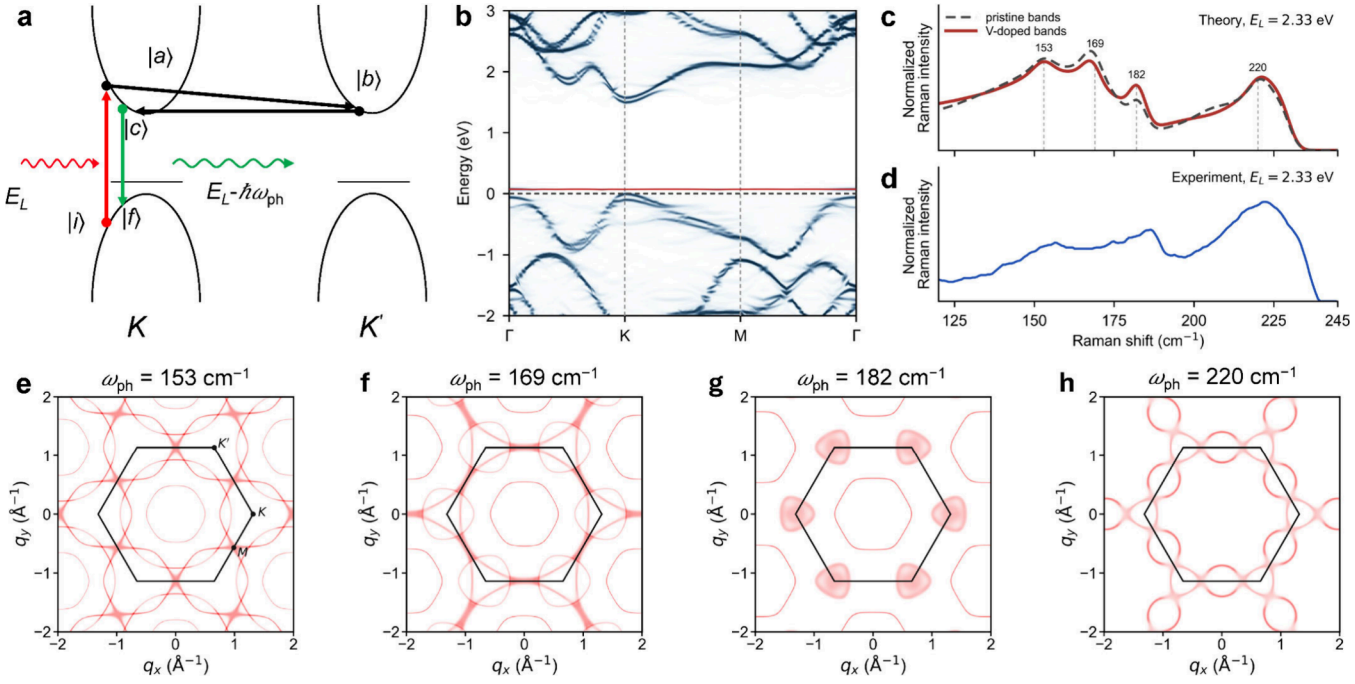


Figure 3. Double-resonance Raman (DRR) process in V-doped monolayer MoS_2. (a) Schematic illustration of the DRR process mediated by phonon-defect scattering, showing the initial (|i⟩), intermediate (|a⟩, |b⟩, |c⟩), and final (|f⟩) electronic states. E_L is the laser energy, and ω_{ph} is the phonon frequency. (b) Unfolded spectral weight (blue) of a 5 × 5 MoS_2 supercell with one V defect. V-induced shallow acceptor level is marked by the red line. (c) Calculated DRR spectra at E_L = 2.33 eV from the pristine (gray dashed line) and V-doped (red solid line). (d) Measured Raman spectrum of V-MoS_2 at the same E_L. (e–h) Phonon-momentum contributions to the DRR spectrum of V-doped MoS_2 at ω_{ph} = 153, 169, 182, and 220 cm^{-1}.

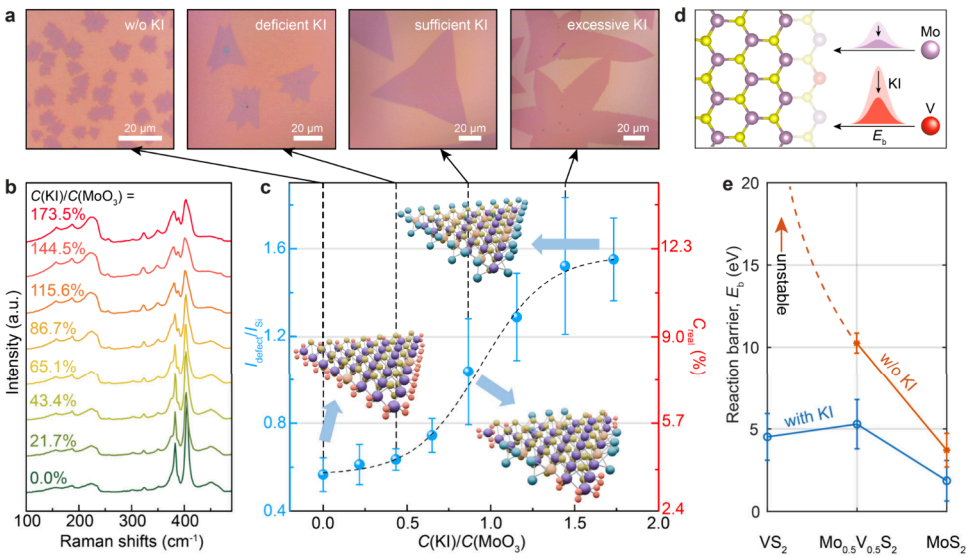


Figure 4. Role of KI in activating V incorporation in the monolayer MoS_2 lattice. (a) From left to right: optical images of the V-MoS_2 flake morphologies grown at constant $C(V_2O_5)/C(MoO_3)$ = 1.03 and increasing C(KI). (b) Raman spectra showing evolution of the defect-associated Raman peaks with increasing $C(KI)/C(MoO_3)$. (c) Normalized I_{defect} and corresponding C_{real} as a function of $C(KI)/C(MoO_3)$. Dashed curve is a Boltzmann sigmoid fitting to the data points. Insets: schematic atomic models for different edge configurations. (d) Schematic illustration of the barrier lowering effect of KI that facilitates V incorporation. (e) EPS model-derived reaction barriers for the growth of VS_2, $Mo_{0.5}V_{0.5}S_2$, and MoS_2 with and without KI. The error bars represent the variation of the reaction barrier when the chemical potential of the passivating species is varied between its two thermodynamic limits under the growth condition considered; the same definition is applied to both the O- and I-passivated cases.

true doping concentration, C_{real}, capturing both the linear and saturation dependence on C_{nom}.

To understand the defect-induced Raman evolution, we calculate the double-resonance Raman (DRR) processes[28] in V-doped monolayer MoS_2. Atomic-scale defects can activate DRR processes through phonon-defect scattering, resulting in the emergent Raman peaks that correspond to zone boundary phonon frequencies (100–250 cm^{-1} for monolayer MoS_2[29,30]). Figure 3a illustrates a specific DRR process where an electron is excited by an incident photon (|i⟩→|a⟩), subsequently scattered by a phonon with nonzero momentum (|a⟩→|b⟩), followed by defect scattering (|b⟩→|

https://doi.org/10.1021/acs.nanolett.6c03019
Nano Lett. XXXX, XXX, XXX−XXX

Downloaded from pubs.acs.org/naletd/article-pdf/doi/10.1021/acs.nanolett.6c03019/6874322/acs.nanolett.6c03019.pdf by SOGANG UNIV user on 06 October 2026

$c\rangle$), and finally recombines with the concomitant hole in the valence band ($|c\rangle \rightarrow |f\rangle$). The defect scattering, as the enabling step for the DRR process, naturally leads the DRR amplitude to be linearly dependent on the defect density, analogous to the D peak of carbon nanomaterials.[31]

Figure 3b shows the unfolded band structure of a 5 × 5 MoS_2 supercell with one substitutional V atom. We find that the V-induced shallow acceptor level lies about 0.07 eV above the valence band maximum (red). Figure 3c shows the DRR spectra at E_L = 2.33 eV calculated from the pristine and V-doped MoS_2 band structures with pristine phonons and constant matrix elements (Supporting Information). Figure 3d presents the measured Raman spectrum at the same excitation energy for comparison (extracted from Figure S7). The calculated DRR spectra show peaks at 153, 169, 182, and 220 cm^{-1} and closely resemble the measured spectrum. Defect-activated peaks in this range have also been reported for Ga-ion-irradiated MoS_2.[32] Figure 3e−h further clarifies the phonon momentum contributions to the Raman peaks found in our DRR spectrum calculations. Specifically, peaks at 153 cm^{-1} and 169 cm^{-1} are predominantly associated with M-point phonons, while the 182 cm^{-1} peak mainly arises from scattering involving K-point phonons. The 220 cm^{-1} peak results from mixed contributions of phonons at different Brillouin zone boundary points. We note that our Raman measurements show a resonant enhancement at E_L = 1.96 eV (Figure S7). The present calculations do not include such resonant excitation where excitons can strongly affect the Raman response. This lies beyond the scope of this work. Nevertheless, the qualitative agreement between the experimental and simulated Raman spectra at E_L = 2.33 eV, combined with atomic-resolution STEM imaging, single-atom EELS, and EELS elemental mapping (Figure 1d−h), supports the origin of the low-frequency Raman features as V substitution. This assignment is further supported by comparing it with the lately reported Raman characteristics of MoS_2 substitutionally doped by other heteroatoms.[33]

The above results justify both experimentally and theoretically that the convoluted low-frequency Raman peaks, closely associated with substitutional V dopants, can be a good probe to the V doping concentration and uniformity. Utilizing this capability, we further explored the detailed role of KI on the doped growth of V-MoS_2. This was achieved by keeping C_{nom} in the supersaturated regime ($C(V_2O_5)/C(MoO_3)$ = 1.03, well beyond the achievable V doping density) so that the evolution of the normalized I_{defect} (C_{real}) can be correlated directly to the varying C(KI). Figure 4a shows morphological evolution of monolayer V-MoS_2 flakes with respect to the change of C(KI). It was found that sufficient C(KI) leads to the formation of larger triangular domains (edge length of up to ∼150 μm), indicative of accelerated growth kinetics. However, excessive KI causes a significant deviation from the common triangular shapes to lobe-like structures (right panel of Figure 4a), demonstrating overly rapid growth and concomitant edge instability.[34] Nevertheless, the uniform I_{defect} distribution was preserved within these monolayer lobes (Figure S8), making I_{defect} still valid as the C_{real} indicator.

Figure 4b exhibits Raman spectra of V-MoS_2 samples grown under varied C(KI). The evolving defect-associated Raman peaks indicate that the saturation doping densities are C(KI)-dependent. We further extracted the normalized I_{defect} (which can be translated into C_{real}) and plotted it versus C(KI) (Figure 4c). An S-shaped relation was revealed between the two, sharing the thermodynamic behavior of a variety of biosystems such as ion channels,[35] whose ionic conductance has S-shaped dependence on membrane potential as well. This comparison is based solely on the mathematical similarity of the sigmoidal response functions. Generally, such dependence can be described by a Boltzmann sigmoid equation, which in our case is written as

$$C_{real} = \frac{C_{min} + C_{max} \exp\left[\frac{S(x - x_0)}{k_B T}\right]}{1 + \exp\left[\frac{S(x - x_0)}{k_B T}\right]} \quad (1)$$

where C_{min} and C_{max} are the lower and upper extrapolated asymptotes for the V-doping density, $x = C(KI)/C(MoO_3)$ is the normalized unitless C(KI), x_0 is the x value to obtain $C_{real} = (C_{max} + C_{min})/2$, $S = -d\Delta F/dx$ is the sensitivity of the free-energy difference between the O- and I-passivated edge states to the KI ratio (see the Supporting Information), and k_BT = 83 meV is the thermal energy at the growth temperature (T = 690 °C). The detailed derivation of eq 1 is provided in the Supporting Information. The fit yielded C_{min} = 3.8%, C_{max} = 12.1%, x_0 = 0.94, and S = 0.42 eV. Alternative sigmoidal functions were also evaluated using the same experimental data set (Tables S3 and S4). The Boltzmann function was retained because it not only yields the highest fitness to experimental data but also offers a physically interpretable description within the proposed two-state EPS framework. Notably, the extracted S = 0.42 eV indicates that the free-energy difference between the O- and I-passivated edge states changes by 0.42 eV per unit x. This redistribution of edge states lowers the effective V−Mo incorporation-barrier difference and thereby activates substitutional doping of V heteroatoms in the monolayer MoS_2 lattice; the barrier difference itself narrows at a rate $\sigma(x)$ that is related to, but numerically distinct from, S (Supporting Information).

The Boltzmann sigmoidal dependence can be facilely understood within the EPS framework, which has successfully explained the Brønsted-Evans−Polanyi relation in halide-activated MoS_2 growth.[24] This model considers chemical passivation of MoS_2 edges by either oxygen (without KI) or iodine atoms (with KI); the formation of a new row of MoS_2 lattice is simply a substitution reaction of oxygen/iodine by sulfur atoms. Mo and V atoms, however, encounter different reaction barriers for incorporation, depending on the edge-passivation states. When changing from oxygen to iodine termination, the V incorporation barrier lowers more significantly than that of Mo (Figure 4d), thereby boosting the V doping density.

Implementing first-principles calculations, we qualitatively validated the above EPS-based mechanistic analysis, as shown in Figure 4e. More calculation details are provided in Figure S9 and the Method Section in Supporting Information; the calculations follow the procedure reported in our previous work.[24] In the case of oxygen termination, the derived reaction barriers increase rapidly with respect to the increasing V concentration on the edge (0% → 50% → 100%), and pure VS_2 edge is thermodynamically unstable when surrounded by oxygen (orange curve in Figure 4e). Once the edge is passivated by iodine atoms, the reaction barriers for all the three cases decrease significantly (blue curve in Figure 4e), supporting the activation effect of KI on the V-doped growth. We note that our calculations considered only the two extreme edge-passivation states, and mixed oxygen/iodine termination should result in reaction barriers between the blue and orange

Downloaded from pubs.acs.org/naletd/article-pdf/doi/10.1021/acs.nanolett.6c03019/6874322/acs.nanolett.6c03019.pdf by SOGANG UNIV user on 06 October 2026

https://doi.org/10.1021/acs.nanolett.6c03019
Nano Lett. XXXX, XXX, XXX−XXX

curves. A natural outcome to this is the Boltzmann sigmoidal relation as observed in Figure 4c, where the lower and upper limits of doping density associate with edges saturated and passivated by oxygen and iodine atoms, respectively. To further assess the role of the halide species, we compared the normalized I_{defect}/I_{Si} responses of V−MoS_2 samples grown with different potassium halide promoters. The marked variation among the tested salts (Figure S10) supports a halide-dependent contribution to the observed activation under the tested conditions. Together, these results provide a plausible and self-consistent iodide-mediated mechanism for doping activation that is consistent with our EPS model, while not excluding a contribution from K^+ ions (for example, by acting as a flux agent that affects precursor spreading and reactivity). Importantly, the sigmoidal dependence exists only because the termination state lowers the V-incorporation barrier more strongly than the Mo barrier; a synchronous reduction of both barriers would leave the V−Mo barrier difference and, hence, the doping density unchanged (Supplementary Note 1).

In summary, this work establishes iodide-activated substitutional doping as a powerful strategy for achieving tunable and uniform vanadium incorporation into monolayer MoS_2. The developed Raman spectroscopic probe, as validated by atomic-resolution STEM characterization, provides a reliable metric for quantifying doping concentration and uniformity, enabling the discovery of a Boltzmann sigmoidal relationship between the KI promoter concentration and the V doping density. This activation mechanism is elegantly explained within the EPS framework and is further supported by first-principles calculations. Our work not only advances the fundamental understanding of doping kinetics in 2D semiconductors but also outlines a generalizable pathway for controlled heteroatom substitutions. The iodide-activated doping paradigm is anticipated to be extended to other TMD systems and dopant species, potentially unlocking new electronic, spintronic, and catalytic applications for tailored 2D materials.

■ ASSOCIATED CONTENT

Supporting Information

The Supporting Information is available free of charge at https://pubs.acs.org/doi/10.1021/acs.nanolett.6c03019.

Details of the experimental and calculation methods, additional STEM images, spectral results, and schematic EPS models (PDF)

■ AUTHOR INFORMATION

Corresponding Authors

Cong Su − *Department of Material Science, Yale University, New Haven, Connecticut 06511, United States; Department of Physics, University of California at Berkeley, Berkeley, California 94720, United States*; Email: cong.su@yale.edu

Young Woo Choi − *Department of Physics, University of California at Berkeley, Berkeley, California 94720, United States; Department of Physics and Center for Nano Materials, Sogang University, Seoul 04107, Korea*; orcid.org/0000-0003-4725-1299; Email: ywchoi02@sogang.ac.kr

Qingqing Ji − *State Key Laboratory of Quantum Functional Materials, School of Physical Science and Technology, ShanghaiTech University, Shanghai 201210, China*; orcid.org/0000-0001-5526-3746; Email: jiqq@shanghaitech.edu.cn

Authors

Yuanyuan Qiu − *State Key Laboratory of Quantum Functional Materials, School of Physical Science and Technology, ShanghaiTech University, Shanghai 201210, China*

Bin Hua − *State Key Laboratory of Quantum Functional Materials, School of Physical Science and Technology, ShanghaiTech University, Shanghai 201210, China*

Zhenping Wang − *Department of Material Science, Yale University, New Haven, Connecticut 06511, United States*; orcid.org/0000-0001-8429-7160

Fei Hu − *State Key Laboratory of Quantum Functional Materials, School of Physical Science and Technology, ShanghaiTech University, Shanghai 201210, China*

Dong Zhang − *State Key Laboratory of Quantum Functional Materials, School of Physical Science and Technology, ShanghaiTech University, Shanghai 201210, China; Shanghai Key Laboratory of High-Resolution Electron Microscopy, ShanghaiTech University, Shanghai 201210, China*

Yang Lu − *State Key Laboratory of Quantum Functional Materials, School of Physical Science and Technology, ShanghaiTech University, Shanghai 201210, China*

Marvin L. Cohen − *Department of Physics, University of California at Berkeley, Berkeley, California 94720, United States*

Alex Zettl − *Department of Physics, University of California at Berkeley, Berkeley, California 94720, United States*

Kecheng Cao − *State Key Laboratory of Quantum Functional Materials, School of Physical Science and Technology, ShanghaiTech University, Shanghai 201210, China; Shanghai Key Laboratory of High-Resolution Electron Microscopy, ShanghaiTech University, Shanghai 201210, China*; orcid.org/0000-0002-7180-7237

Complete contact information is available at: https://pubs.acs.org/10.1021/acs.nanolett.6c03019

Author Contributions

#Y.Q., B.H., Z.W., and F.H. contributed equally to this work. Q.J. and C.S. conceived and supervised the project. Y.Q. performed the experiments with assistance from B.H., Z.W., F.H., Y.L., and D.Z. Y.W.C. performed the Raman spectrum calculations. The manuscript was written through contributions of all authors. All authors have given approval to the final version of the manuscript.

Notes

The authors declare no competing financial interest.

■ ACKNOWLEDGMENTS

Q.J. acknowledges the financial support from the National Key R&D Program of China (2024YFA1410500), the Science and Technology Commission of Shanghai Municipality (25JC3200500), and the Startup Fund and the Double First-Class Initiative Fund of ShanghaiTech University. M.L.C. and Y.W.C. acknowledge the support of National Science Foundation (NSF) Grant No. DMR-2325410, and Y.W.C. acknowledges support from the National Research Foundation of Korea (NRF) grant (No. RS-2024-00441954). This work used Stampede3 at TACC through allocation MCA94P030 from the ACCESS program, which is supported by U.S.

https://doi.org/10.1021/acs.nanolett.6c03019
Nano Lett. XXXX, XXX, XXX−XXX

Downloaded from pubs.acs.org/naletd/article-pdf/doi/10.1021/acs.nanolett.6c03019/6874322/acs.nanolett.6c03019.pdf by SOGANG UNIV user on 06 October 2026

National Science Foundation grants #2138259, #2138286, #2138307, #2137603, and #2138296.

REFERENCES

(1) Fahey, P. M.; Griffin, P. B.; Plummer, J. D. Point Defects and Dopant Diffusion in Silicon. *Rev. Mod. Phys.* **1989**, *61* (2), 289−384.
(2) Norris, D. J.; Efros, A. L.; Erwin, S. C. Doped Nanocrystals. *Science* **2008**, *319* (5871), 1776−1779.
(3) Wei, X.; Zhang, P.; Xu, T.; Zhou, H.; Bai, Y.; Chen, Q. Chemical Approaches for Electronic Doping in Photovoltaic Materials beyond Crystalline Silicon. *Chem. Soc. Rev.* **2022**, *51* (24), 10016−10063.
(4) Zhao, Y.; Xu, K.; Pan, F.; Zhou, C.; Zhou, F.; Chai, Y. Doping, Contact and Interface Engineering of Two-Dimensional Layered Transition Metal Dichalcogenides Transistors. *Adv. Funct. Mater.* **2017**, *27* (19), 1603484.
(5) Loh, L.; Zhang, Z.; Bosman, M.; Eda, G. Substitutional Doping in 2D Transition Metal Dichalcogenides. *Nano Res.* **2021**, *14* (6), 1668−1681.
(6) Chhowalla, M.; Jena, D.; Zhang, H. Two-Dimensional Semiconductors for Transistors. *Nat. Rev. Mater.* **2016**, *1* (11), 16052.
(7) Lu, Y.; Li, C.; Yang, S.; Yuan, M.; Qiao, S.; Ji, Q. Dopant-Mediated Carrier Tunneling in Short-Channel Two-Dimensional Transistors. *Mater. Chem. Front.* **2024**, *8*, 3300−3307.
(8) Liu, Y.; Duan, X.; Shin, H.; Park, S.; Huang, Y.; Duan, X. Promises and Prospects of Two-Dimensional Transistors. *Nature* **2021**, *591*, 43−53.
(9) Kim, K. S.; Kwon, J.; Ryu, H.; Kim, C.; Kim, H.; Lee, E.-K.; Lee, D.; Seo, S.; Han, N. M.; Suh, J. M.; Kim, J.; Song, M.-K.; Lee, S.; Seol, M.; Kim, J. The Future of Two-Dimensional Semiconductors beyond Moore's Law. *Nat. Nanotechnol.* **2024**, *19* (7), 895−906.
(10) Gao, Y.; Ganguli, N.; Kelly, P. J. DFT Study of Itinerant Ferromagnetism in p-Doped Monolayers of MoS_2. *Phys. Rev. B* **2019**, *100* (23), 235440.
(11) Gao, Y.; Ganguli, N.; Kelly, P. J. Itinerant Ferromagnetism in p-Doped Monolayers of MoS_2. *Phys. Rev. B* **2019**, *99* (22), 220406.
(12) Duong, D. L.; Yun, S. J.; Kim, Y.; Kim, S.-G.; Lee, Y. H. Long-Range Ferromagnetic Ordering in Vanadium-Doped WSe_2 Semiconductor. *Appl. Phys. Lett.* **2019**, *115* (24), 242406.
(13) Yun, S. J.; Duong, D. L.; Ha, D. M.; Singh, K.; Phan, T. L.; Choi, W.; Kim, Y.; Lee, Y. H. Ferromagnetic Order at Room Temperature in Monolayer WSe_2 Semiconductor via Vanadium Dopant. *Adv. Sci.* **2020**, *7* (9), 1903076.
(14) Song, B.; Yun, S. J.; Jiang, J.; Avila, J.; Beach, K.; Choi, W.; Kim, Y.-M.; Yoon, D.; Terrones, H.; Song, Y. J.; Asensio, M. C.; Duong, D. L.; Lee, Y. H. Evidence of Itinerant Holes for Long-Range Magnetic Order in the Tungsten Diselenide Semiconductor with Vanadium Dopants. *Phys. Rev. B* **2021**, *103* (9), 094432.
(15) Zou, J.; Cai, Z.; Lai, Y.; Tan, J.; Zhang, R.; Feng, S.; Wang, G.; Lin, J.; Liu, B.; Cheng, H.-M. Doping Concentration Modulation in Vanadium-Doped Monolayer Molybdenum Disulfide for Synaptic Transistors. *ACS Nano* **2021**, *15* (4), 7340−7347.
(16) Gao, B.; Yan, Y.; Zhang, S.; Wu, Z.; Meng, Y.; Zhang, Y.; Wang, W.; Shen, Y.; Hu, S.; Li, B.; Shao, H.; Xie, P.; Yip, S.; Ho, J. C. Precise p-Type Substitutional Doping Enables WS_2 p-n Anti-Ambipolar Homojunction Phototransistor Arrays. *Adv. Funct. Mater.* **2025**, *35* (33), 2425884.
(17) Nguyen, L.-A. T.; Jiang, J.; Nguyen, T. D.; Kim, P.; Joo, M.-K.; Duong, D. L.; Lee, Y. H. Electrically Tunable Magnetic Fluctuations in Multilayered Vanadium-Doped Tungsten Diselenide. *Nat. Electron.* **2023**, *6* (8), 582−589.
(18) Dearnaley, G. Ion Implantation. *Nature* **1975**, *256*, 701−705.
(19) Murai, Y.; Zhang, S.; Hotta, T.; Liu, Z.; Endo, T.; Shimizu, H.; Miyata, Y.; Irisawa, T.; Gao, Y.; Maruyama, M.; Okada, S.; Mogi, H.; Sato, T.; Yoshida, S.; Shigekawa, H.; Taniguchi, T.; Watanabe, K.; Canton-Vitoria, R.; Kitaura, R. Versatile Post-Doping toward Two-Dimensional Semiconductors. *ACS Nano* **2021**, *15* (12), 19225−19232.
(20) Zhang, T.; Fujisawa, K.; Zhang, F.; Liu, M.; Lucking, M. C.; Gontijo, R. N.; Lei, Y.; Liu, H.; Crust, K.; Granzier-Nakajima, T.; Terrones, H.; Elías, A. L.; Terrones, M. Universal *In Situ* Substitutional Doping of Transition Metal Dichalcogenides by Liquid-Phase Precursor-Assisted Synthesis. *ACS Nano* **2020**, *14* (4), 4326−4335.
(21) Gao, H.; Suh, J.; Cao, M. C.; Joe, A. Y.; Mujid, F.; Lee, K.-H.; Xie, S.; Poddar, P.; Lee, J.-U.; Kang, K.; Kim, P.; Muller, D. A.; Park, J. Tuning Electrical Conductance of MoS_2 Monolayers through Substitutional Doping. *Nano Lett.* **2020**, *20* (6), 4095−4101.
(22) Li, S.; Wang, S.; Tang, D.-M.; Zhao, W.; Xu, H.; Chu, L.; Bando, Y.; Golberg, D.; Eda, G. Halide-Assisted Atmospheric Pressure Growth of Large WSe_2 and WS_2 Monolayer Crystals. *Appl. Mater. Today* **2015**, *1* (1), 60−66.
(23) Zhou, J.; Lin, J.; Huang, X.; Zhou, Y.; Chen, Y.; Xia, J.; Wang, H.; Xie, Y.; Yu, H.; Lei, J.; Wu, D.; Liu, F.; Fu, Q.; Zeng, Q.; Hsu, C.-H.; Yang, C.; Lu, L.; Yu, T.; Shen, Z.; Lin, H.; Yakobson, B. I.; Liu, Q.; Suenaga, K.; Liu, G.; Liu, Z. A Library of Atomically Thin Metal Chalcogenides. *Nature* **2018**, *556* (7701), 355−359.
(24) Ji, Q.; Su, C.; Mao, N.; Tian, X.; Idrobo, J.-C.; Miao, J.; Tisdale, W. A.; Zettl, A.; Li, J.; Kong, J. Revealing the Brønsted-Evans-Polanyi Relation in Halide-Activated Fast MoS_2 Growth toward Millimeter-Sized 2D Crystals. *Sci. Adv.* **2021**, *7* (44), No. eabj3274.
(25) Lin, X. W.; Wang, Y. Y.; Dravid, V. P.; Michalakos, P. M.; Kung, M. C. Valence States and Hybridization in Vanadium Oxide Systems Investigated by Transmission Electron-Energy-Loss Spectroscopy. *Phys. Rev. B* **1993**, *47* (7), 3477−3481.
(26) Zhang, Y.; Wang, Y.; Wu, Y.; Shu, X.; Zhang, F.; Peng, H.; Shen, S.; Ogawa, N.; Zhu, J.; Yu, P. Artificially Controlled Nanoscale Chemical Reduction in VO_2 through Electron Beam Illumination. *Nat. Commun.* **2023**, *14* (1), 4012.
(27) Kim, H.; Ovchinnikov, D.; Deiana, D.; Unuchek, D.; Kis, A. Suppressing Nucleation in Metal-Organic Chemical Vapor Deposition of MoS_2 Monolayers by Alkali Metal Halides. *Nano Lett.* **2017**, *17* (8), 5056−5063.
(28) Carvalho, B. R.; Wang, Y.; Mignuzzi, S.; Roy, D.; Terrones, M.; Fantini, C.; Crespi, V. H.; Malard, L. M.; Pimenta, M. A. Intervalley Scattering by Acoustic Phonons in Two-Dimensional MoS_2 Revealed by Double-Resonance Raman Spectroscopy. *Nat. Commun.* **2017**, *8* (1), 14670.
(29) Mignuzzi, S.; Pollard, A. J.; Bonini, N.; Brennan, B.; Gilmore, I. S.; Pimenta, M. A.; Richards, D.; Roy, D. Effect of Disorder on Raman Scattering of Single-Layer MoS_2. *Phys. Rev. B* **2015**, *91* (19), 195411.
(30) Wang, Z.; Zhao, G.; Luo, R.; Johnson, I.; Kashani, H.; Chen, M. Chemical Doping Induced Zone-Edge Phonon Renormalization in Single-Layer MoS_2. *Phys. Rev. B* **2019**, *100* (8), 085401.
(31) Venezuela, P.; Lazzeri, M.; Mauri, F. Theory of Double-Resonant Raman Spectra in Graphene: Intensity and Line Shape of Defect-Induced and Two-Phonon Bands. *Phys. Rev. B* **2011**, *84* (3), 035433.
(32) Fujisawa, K.; Carvalho, B. R.; Zhang, T.; Perea-López, N.; Lin, Z.; Carozo, V.; Ramos, S. L. L. M.; Kahn, E.; Bolotsky, A.; Liu, H.; Elías, A. L.; Terrones, M. Quantification and Healing of Defects in Atomically Thin Molybdenum Disulfide: Beyond the Controlled Creation of Atomic Defects. *ACS Nano* **2021**, *15* (6), 9658−9669.
(33) Urooj, Z.; Li, Y.; Mao, J.; Sun, H.; Tan, T.; Qi, J.; Wu, J.; Zheng, Q.; Abbas, T.; Younas, M.; Wang, H.; Chen, Y.; Suenaga, K.; Xie, L. Experimentally Mapping the Elemental Doping of MoS_2 Monolayer. *Adv. Mater.* **2026**, *38* (20), No. e22574.
(34) Huang, L.; Thi, Q. H.; Zheng, F.; Chen, X.; Chu, Y. W.; Lee, C.-S.; Zhao, J.; Ly, T. H. Catalyzed Kinetic Growth in Two-Dimensional MoS_2. *J. Am. Chem. Soc.* **2020**, *142* (30), 13130−13135.
(35) Dubois, J.-M.; Ouanounou, G.; Rouzaire-Dubois, B. The Boltzmann Equation in Molecular Biology. *Prog. Biophys. Mol. Biol.* **2009**, *99* (2−3), 87−93.

Downloaded from pubs.acs.org/naletd/article-pdf/doi/10.1021/acs.nanolett.6c03019/6874322/acs.nanolett.6c03019.pdf by SOGANG UNIV user on 06 October 2026

https://doi.org/10.1021/acs.nanolett.6c03019
Nano Lett. XXXX, XXX, XXX−XXX